Schweizerische Eidgenossenschaft
Confédération suisse
Confederazione Svizzera
Confederaziun svizra

Federal Department of the Environment, Transport, Energy and Communications DETEC

Swiss Federal Office of Energy SFOE
Energy Research and Cleantech Division

REEL Demo – Romande Energie ELectric network in local balance Demonstrator

Deliverable: 4f1 Definition of Schemes and Needed Coordination for the Provision of Ancillary Services from Small Distributed Resources

Demo site: Aigle

Developed by
Mohsen Kalantar Neyestanaki, EPFL-PWRS
Fabrizio Sossan, EPFL-DESL
Rachid Cherkaoui, EPFL-PWRS
in collaboration with
Swissgrid

[Lausanne, 29.11.2018]

Table of Contents

Nomenclature

Indices and sets

0′,0	Index for MV/LV common coupling nodes of ADN that connect ADN to the upper-layer grid.
f	Index for the linear boundaries modeling the maximum current flow limit of a branch.
h	Index for Dispatchable distributed generators (DDGs).
i, j	Index for nodes excluding $0'$.
k	Index for stochastic distributed generators (SDGs).
l	Index for branches.
n	Index for the linear boundaries modeling the capability curve of a DDG/SDG.
s	Index for scenarios.
t	Index for time intervals.
$\mathbb{B}$	Set of nodes of ADN excluding $0'$.
$\mathbb{DG}$	Set of DDGs of ADN.
$\mathbb{DG}_i$	Set of DDGs connected to node *i*.
$\mathbb{F}_l$	Set of the linear boundaries modeling the maximum current flow limit of branch *l*.
$\mathbb{L}$	Set of branches of ADN.
$N_{\mathbb{B}}$	Number of nodes of ADN excluding $0'$.
$\mathbb{C}_h, \mathbb{C}_k$	Set of linear boundaries modeling the capability curve of DDG *h*/ SDG *k*.
$\mathbb{SG}_i$	Set of SDGs connected to node *i*.
$\mathbb{S}$	Set of selected credible scenarios.
ψ	Set of optimization variables.
$\Omega(\psi)$, $\Gamma(\psi)$	Set of inequality/equality constraints modeling the operational constraints of ADN and DERs.

Parameters

$\mathrm{a}^{\mathrm{P}}, \mathrm{a}^{\mathrm{Q}}$	Constant terms defining the search direction in $R^{\mathrm{P}}_{0't} - R^{\mathrm{Q}}_{0't}$ coordinate plane.
$\mathbf{E}^{0}_{jt}, \mathbf{E}^{\mathrm{P}}_{jit}, \mathbf{E}^{\mathrm{Q}}_{jit}$	Constant terms of linear function expressing V_{jts} based on $\Delta P^{\mathrm{Net}}_{its}$ and $\Delta Q^{\mathrm{Net}}_{its}$.
$\mathbf{F}^{0}_{fl}, \mathbf{F}^{\mathrm{real}}_{fl}, \mathbf{F}^{\mathrm{imag}}_{fl}$	Constant terms of the linear functions ($f \in \mathbb{F}_l$) modeling the maximum current flow limit of branch *l* based on I^{real}_{lts} and I^{imag}_{lts}.
$\mathbf{G}^{\mathrm{P0}}_{t}, \mathbf{G}^{\mathrm{PP}}_{it}, \mathbf{G}^{\mathrm{PQ}}_{it}$	Constant terms of the linear function expressing $r^{\mathrm{P}}_{0'ts}$ based on $\Delta P^{\mathrm{Net}}_{its}$ and $\Delta Q^{\mathrm{Net}}_{its}$.
$\mathbf{G}^{\mathrm{Q0}}_{t}, \mathbf{G}^{\mathrm{QP}}_{it}, \mathbf{G}^{\mathrm{QQ}}_{it}$	Constant terms of the linear function expressing $r^{\mathrm{Q}}_{0'ts}$ based on $\Delta P^{\mathrm{Net}}_{its}$ and $\Delta Q^{\mathrm{Net}}_{its}$.
$\mathbf{H}^{0,\mathrm{real}}_{lt}, \mathbf{H}^{\mathrm{P,real}}_{lit}, \mathbf{H}^{\mathrm{Q,real}}_{lit}$	Constant terms of the linear function expressing I^{real}_{lts} based on $\Delta P^{\mathrm{Net}}_{its}$ and $\Delta Q^{\mathrm{Net}}_{its}$.
$\mathbf{H}^{0,\mathrm{imag}}_{lt}, \mathbf{H}^{\mathrm{P,imag}}_{lit}, \mathbf{H}^{\mathrm{Q,imag}}_{lit}$	Constant terms of the linear function expressing I^{imag}_{lts} based on $\Delta P^{\mathrm{Net}}_{its}$ and $\Delta Q^{\mathrm{Net}}_{its}$.
$\mathrm{I}^{\mathrm{Max}}_{l}$	Maximum current limit of the branch l $[p.u.]$.
$\mathbf{K}^{0}_{nht}, \mathbf{K}^{\mathrm{P}}_{nh}, \mathbf{K}^{\mathrm{Q}}_{nh}$	Constant terms of the linear functions ($n \in \mathbb{C}_h$) modeling the capability curve of DDG *h* based on $r^{\mathrm{P,DG}}_{hts}$ and $r^{\mathrm{Q,DG}}_{hts}$.
$\mathbf{M}^{0}_{nkt}, \mathbf{M}^{\mathrm{P}}_{nk}, \mathbf{M}^{\mathrm{Q}}_{nk}$	Constant terms of the linear functions ($n \in \mathbb{C}_k$) modeling the capability curve of SDG *k* based on $\Delta \mathrm{P}^{\mathrm{SG}}_{kts}$ and $r^{\mathrm{Q,SG}}_{kts}$.

$\mathrm{P}_{0't}^{\mathrm{Base}}, \mathrm{Q}_{0't}^{\mathrm{Base}}$	Active/reactive power absorbed by ADN at its connection point during time slot *t* for the base case operating point (a day-ahead forecasted operating point) $[p.u.]$.
$\mathrm{P}_{it}^{\mathrm{Base}}, \mathrm{Q}_{it}^{\mathrm{Base}}$	Total active/reactive power injected at node *i* during time slot *t* for the base case operating point (a day-ahead forecasted operating point) $[p.u.]$.
$\Delta\mathrm{P}_{its}^{\mathrm{D}}, \Delta\mathrm{Q}_{its}^{\mathrm{D}}$	Deviation of the active/reactive power consumption of the load connected to node *i* from its base case operating point (a day-ahead forecasted operating point) during time slot *t* and scenario *s* $[p.u.]$.
$\Delta\mathrm{P}_{kts}^{\mathrm{SG}}$	Deviation of the active power generation of SDG *k* from its base case operating point (a day-ahead forecasted operating point) during time slot *t* and scenario *s* $[p.u.]$.
$\mathrm{V}_{j}^{\mathrm{Max}}$	Maximum voltage limit of the node *j* $[p.u.]$.
$\mathrm{V}_{j}^{\mathrm{Min}}$	Minimum voltage limit of the node *j* $[p.u.]$.
θ	The angle between the selected direction and $R_{0't}^{\mathrm{P}}$ axis.

Variables

I_{lts}	Current phasor of branch *l* during time slot *t* and scenario *s* $[p.u.]$.
$I_{lts}^{\mathrm{real}}, r_{lts}^{\mathrm{imag}}$	Real/imaginary part of I_{lts} $[p.u.]$.
$\lvert I_{lts}\rvert$	Magnitude of I_{lts} $[p.u.]$.
$r_{0'ts}^{\mathrm{P}}, r_{0'ts}^{\mathrm{Q}}$	Active/reactive power reserve absorbed by ADN from the upper layer grid during time slot *t* and scenario *s* $[p.u.]$.
$r_{hts}^{\mathrm{DG,P}}, r_{hts}^{\mathrm{DG,Q}}$	Active/reactive power reserve injected by DDG *h* to the grid during time slot *t* and scenario *s* $[p.u.]$.
$r_{kts}^{\mathrm{SG,Q}}$	Reactive power reserve injected by SDG *k* to the grid during time slot *t* and scenario *s* $[p.u.]$.
$R_{0't}^{\mathrm{P}}, R_{0't}^{\mathrm{Q}}$	Active/reactive power reserve capacity absorbed by ADN from the upper layer grid during time slot *t* $[p.u.]$.
$P_{0'ts}^{\mathrm{Net}}, Q_{0'ts}^{\mathrm{Net}}$	Total active/reactive power absorbed by ADN at its connection point during time slot *t* and scenario *s* $[p.u.]$.
$\Delta P_{its}^{\mathrm{Net}}, \Delta Q_{its}^{\mathrm{Net}}$	Net deviation of the active/reactive power injection at node *i* from its base case operating point (a day-ahead forecasted operating point) during time slot *t* and scenario *s* $[p.u.]$.
V_{jts}	Voltage magnitude of node *j* during time slot *t* and scenario *s* $[p.u.]$.

1. Description of deliverable and goal

1.1. Executive summary

Distributed energy resources (DERs) installed in active distribution networks (ADNs) can be exploited to provide both active and reactive power reserves to the upper-layer grid (i.e., sub-transmission and transmission systems) at their connection point. This report introduces a method to determine the capability area of an ADN for the provision of both active and reactive power reserves while considering the forecast errors of loads and stochastic generation, as well as the operational constraints of the grid and DERs. The method leverages a linearized load flow model and introduces a set of linear robust optimization problems to estimate the reserve provision capability (RPC) area of the ADN. It is proved that, under certain assumptions, the RPC area is convex. The performance of the proposed method is tested on a modified version of the IEEE 33-bus distribution test system.

1.2. Research question

Environmental concerns and recent developments in renewable energy technologies are leading towards replacing centralized conventional generation in favor of decentralized renewable generation [1]. The main challenge in the way of this transition is the increasing demand for controllable resources to be deployed to guarantee the frequency stability, voltage regulation, power quality, and congestion management, while the magnitudes of conventional ancillary services providers are decreasing [2]-[4].

On the other hand, the number of distributed energy resources (DERs) is progressively increasing in active distribution networks (ADNs). A promising solution to preserve the quality/security of supply is aggregating the flexibility of DERs located in ADNs to provide active/reactive power reserves to the upper-layer grid [5]-[8]. In this emerging architecture, further cooperation between operators of different levels of electric power systems, e.g., transmission system operators (TSOs) and distribution system operators (DSOs), is required to exchange flexibility [9]. Flexibility can be perceived as a service, like active/reactive power reserves, that a resource provides to the grid by adjusting its operating point [7], [10]. The question that arises is:

- how much are the maximum active/reactive power reserves which an ADN can provide upon request at its connecting point to the upper-layer grid?

In this context, the reserve provision capability (RPC) curve of an ADN is defined as a curve characterizing the extreme amount of active and reactive power reserves that ADN can provide to the upper-layer grid. The area surrounded by the RPC curve is called RPC area.

1.3. Novelty of the proposed solutions compared to the state-of-art

All available approaches [5]-[8] suffer from the following limitations:

- they do not model uncertainties. As known, renewable generation and demand at high level of disaggregation is highly volatile. Consequently, these methods can only forecast the RPC area of ADN for short-term horizons (i.e., few minutes ahead), where uncertainties can be neglected. As typical power systems operations entail scheduling operation on longer time horizons (e.g. day-ahead and hours-ahead), accounting for uncertainties is key to achieve a reliable estimation of the RPC;
- they model the RPC area of DERs as a square area, which is unrealistic;
- they entail a high computational effort when the number of DERs is large.

The limitations found in [5]-[8] inspired the content of this paper, that describes a tractable algorithm based on a linear robust optimization problem to estimate the curve and the area of the RPC of an ADN while considering grid constraints and uncertainties of loads and stochastic generation. Grid constraints are modelled by leveraging recent advancements in linearized load flow models [11], whereas uncertainty of loads and stochastic generation are explicitly modelled with scenarios, which are used to enforce robust grid constraints and deliver realistic estimates of the RPC area. To comply with the current scheduling/operation paradigm of current power systems, the proposed method is applied to day-ahead scheduling, where uncertainties play a salient role. This longer-term horizon method, compared to existing ones, entails considering a large number of scenarios to model the forecasting errors of demand and stochastic generation. It is shown that the proposed method can compute robust estimates of the RPC of ADNs in a reliable and efficient way.

1.4. Description

1.4.1. Problem Statement

Although specifications might vary from system to system, the procedure to allocate power reserve in electrical grids generally consists of two steps:

1-**Reserve capacity booking**: This step is usually carried out the day before real-time grid operations. For each time slot of the next day, the TSO estimates its needs for reserves, and reserve providers estimate their capacity for providing reserve. Then, demand and offers are collected in the day-ahead reserve market and the TSO books its required reserves by clearing the market. In this stage, no real product is exchanged between the TSO and reserve providers.

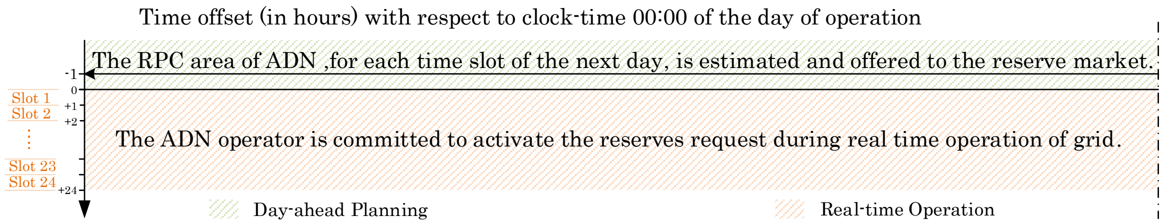

Fig. 1. Day-ahead procedure for estimating the ADN's RPC area.

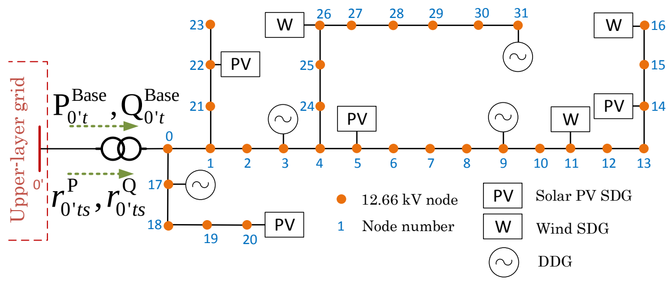

Fig. 2. The modified IEEE 33-bus distribution test system.

2-**Reserve activation**: This step is carried out during the real-time operation. In case of need, the TSO sends its requests to the reserve providers who already succeeded to sell their reserve capacities in the reserve market. Then, those reserve providers activate all/a portion of the reserve capacities they have sold.

This deliverable focuses on the first step and in line with this procedure, it presents a method to estimate the RPC area of an ADN for each individual time slot of the next day so that it can be offered to the day-ahead reserve market, according to the sequence of operation shown in the timeline of Fig. 1. Without losing generality, it is considered that:

- the RPC area of an ADN for each time slot of the next day is estimated one hour before the beginning of the next day;
- the next day consists of 24 time slots with 1-hour duration.

Despite day-ahead scheduling is specifically targeted, the proposed formulation is generic and can accommodate any scheduling horizon by plugging-in suitable forecasts. Finally, it is worth to notice that the RPC areas at various time slots are determined separately and in the same manner. They are independent from each other. For this reason, the formulation in the next section refers to one time slot only, and it is applied identically for the whole time horizon.

Although references to the distribution grid of Fig. 2 are made throughout the paper, the proposed formulation can accommodate any kind of grid (i.e., meshed or radial) with a single connection point to the upper-layer grid.

1.4.2. Method

The power flow at the connection point of the grid in Fig. 2 is:

$$P_{0'ts}^{\text{Net}} = \text{P}_{0't}^{\text{Base}} + r_{0'ts}^{\text{P}}, \tag{1}$$

$$Q_{0'ts}^{\text{Net}} = \text{Q}_{0't}^{\text{Base}} + r_{0'ts}^{\text{Q}}. \tag{2}$$

The proposed method consists of three main parts: definition of the search directions, computation of the points of the RPC curve along the defined search directions, and estimation of the whole RPC curve. The three parts are explained in the following by referring to Fig. 3, that exemplifies the RPC on the $R_{0't}^{\text{P}} - R_{0't}^{\text{Q}}$ plane.

1. **Definition of the search directions:** As shown in Fig. 3, the angle θ defines a search direction in the $R_{0't}^{\text{P}} - R_{0't}^{\text{Q}}$ plane and can take a value between 0° and 360°. It determines a_{P} and a_{Q} as follows:

$$\text{a}_{\text{p}} = \begin{cases} -1 & 0° \leq \theta < 90° \\ +1 & 90° < \theta < 270° \\ -1 & 270° < \theta < 360°. \end{cases} \tag{3}$$

$$\text{a}_{\text{Q}} = \tan(\theta) \qquad 0° \leq \theta < 360°. \tag{4}$$

a_{P} and a_{Q} are used in the second step, when solving the linear robust optimization problem. A set of search directions is defined with the following procedure:

A. The minimum acceptable granularity for the final estimated RPC curve is defined. It determines the procedure termination criterion. The procedure is terminated when the Euclidean distances between two consecutive estimated points on the RPC curve (yellow squares in **Error! Reference source not found.**) are smaller than the defined granularity.

B. Four search directions, corresponding to $\theta = 0°, 90°, 180°, 270°$, are defined. For each search direction, the linear robust optimization problem introduced in step 2 is solved, determining 4 points on the RPC curve.

C. The search directions are ordered based on their θ.

D. The Euclidean distance between each couple of consecutive points for increasing θ on the RPC curve is calculated. If all the distances are smaller than the defined granularity in A, the procedure ends and goes to final step 3; otherwise, the couple of consecutive points with the largest distance is selected, and the arithmetic mean of their search direction θ is used as the new search direction.

E. For the new search direction in D, the linear robust optimization problem of step 2, is solved.

F. Jump to C.

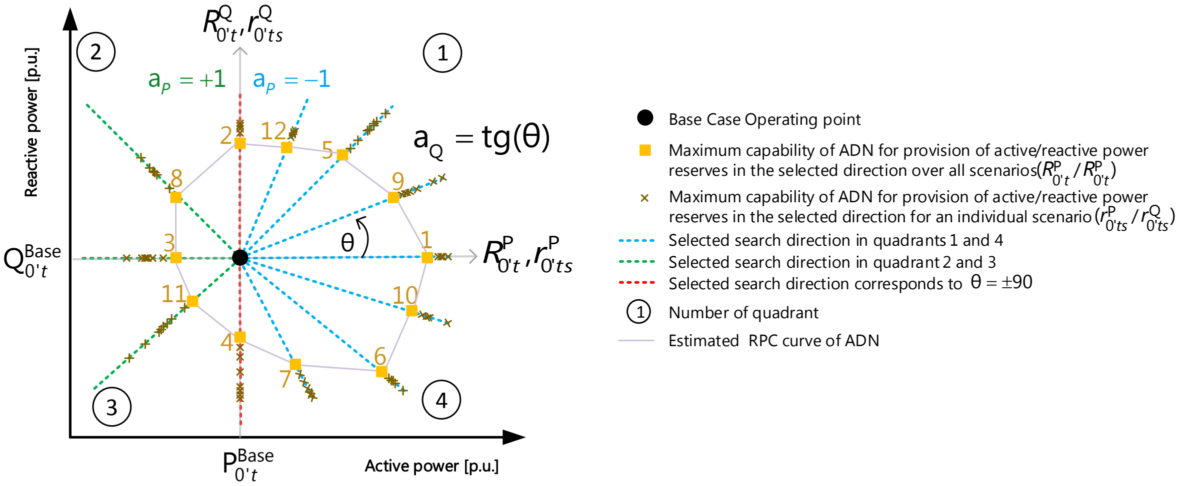

Fig. 3. Typical estimated RPC area of an ADN.

The abovementioned procedure is illustrated in Fig. 3, where the numbers on the RPC curve denote the sequence of the defined directions.

2. **Computation of the points of the RPC curve along the defined search directions:** For a defined θ, this step entails solving the optimization problem detailed in Section 1.4.3 to find the point on the RPC curve associated to that search direction.
3. **Estimation of the whole RPC curve:** Once the points of the RPC curve are defined, they are linearly interpolated to approximate the whole RPC curve, as shown in Fig. 3. As discussed and formally proven in Appendix, this is a valid approximation because the RPC curve determined by this method is convex by construction.

1.4.3. Linear Robust Optimization Problem Formulation

1.4.3.1. Mathematical Formulation

This section describes the linear robust optimization problem that determines a point on the RPC curve for a selected search direction. Assuming $\theta \neq 90°, 180°$, coefficients a_P and a_Q are respectively calculated based on (3) and (4). The associated point of the RPC curve is calculated by solving the following optimization problem:

$$\min_{\psi} \; a_P R^{P}_{0't} \tag{5}$$

subject to

$$r^{Q}_{0'ts} = a_Q r^{P}_{0'ts} \qquad \forall s \in \mathbb{S}, \tag{6}$$

$$a_P r^{P}_{0'ts} \leq a_P R^{P}_{0't} \leq 0 \qquad \forall s \in \mathbb{S}, \tag{7}$$

$R^{\mathrm{Q}}_{0'{t}} = \mathrm{a_Q} R^{\mathrm{P}}_{0'{t}}$ $\forall s \in \mathbb{S},$ (8)

$\Omega(\psi) \leq 0$ $\forall s \in \mathbb{S},$ (9)

$\Gamma(\psi) = 0$ $\forall s \in \mathbb{S}.$ (10)

For $\mathrm{a_P} = -1$, the objective function (5) minimizes $-R^{\mathrm{P}}_{0'{t}}$ or equivalently maximizes $R^{\mathrm{P}}_{0'{t}}$, whereas, for $\mathrm{a_P} = +1$, it minimizes $R^{\mathrm{P}}_{0'{t}}$. Constraint (6) specifies the search direction in the $R^{\mathrm{P}}_{0'{t}} - R^{\mathrm{Q}}_{0'{t}}$ plane, as shown in Fig. 3. Since the cost function (5) consists of the active power reserve capacity $R^{\mathrm{P}}_{0'{t}}$ only, constraint (6) achieves to steer the search in the direction of the $R^{\mathrm{Q}}_{0'{t}}$ axis also. In order to guarantee that the ADN can provide, in real time operation, any amount of reserve corresponding to the points located in its RPC area in spite of uncertainties, this method computes robust estimates of the points on the RPC curve. In other words, $R^{\mathrm{P}}_{0'{t}}$ and $R^{\mathrm{Q}}_{0'{t}}$ (i.e., yellow squares in Fig. 3) are chosen as the most conservative $r^{\mathrm{P}}_{0'{ts}} and\ r^{\mathrm{Q}}_{0'{ts}}$ (i.e., the innermost grey crosses in Fig. 3). This is achieved by constraints (7) and (8). In (7), $\mathrm{a_P} = -1$ corresponds to the quadrants 1 and 4 (positive values of $r^{\mathrm{P}}_{0'{ts}}$ and $R^{\mathrm{P}}_{0'{t}}$), whereas $\mathrm{a_P} = +1$ corresponds to the quadrants 2 and 3 (negative values of $r^{\mathrm{P}}_{0'{ts}}$ and $R^{\mathrm{P}}_{0'{t}}$). Thanks to (6) and (7), the abovementioned conservative manner for $R^{\mathrm{Q}}_{0'{t}}$ in particular can be modeled as constraint (8).

For search directions $\theta = 90°, 180°$, the objective function and constraints (5)-(8) are modifies as:

$\min\limits_{\psi}\ \mathrm{a}' R^{\mathrm{Q}}_{0'{t}}$ (5′)

subject to

$r^{\mathrm{p}}_{0'{ts}} = 0$ $\forall s \in \mathbb{S},$ (6′)

$\mathrm{a}' r^{\mathrm{Q}}_{0'{ts}} \leq \mathrm{a}' R^{\mathrm{Q}}_{0'{t}} \leq 0$ $\forall s \in \mathbb{S},$ (7′)

$R^{\mathrm{P}}_{0'{t}} = 0$ $\forall s \in \mathbb{S},$ (8′)

in (5′)-(8′), a' is equal to -1 and +1 for $\theta = 90°$ and $\theta = 180°$, respectively.

Expressions (9) and (10) are linear and model the operational constraints of ADN and DERs, as described in subsections 1.4.3.2 and 1.4.3.3. Symbol ψ defines the optimization variables of the problem as:

$\psi = \{R^{\mathrm{P}}_{0'{t}}, R^{\mathrm{Q}}_{0'{t}}, r^{\mathrm{P}}_{0'{ts}}, r^{\mathrm{Q}}_{0'{ts}}, I^{\mathrm{real}}_{lts}, I^{\mathrm{imag}}_{lts}, V_{jts}, r^{\mathrm{DG,P}}_{hts}, r^{\mathrm{DG,Q}}_{hts}, r^{\mathrm{SG,Q}}_{kts}\}.$

The problem (5)-(10) is a linear robust optimization problem that determines the point on the RPC curve associated to search direction θ.

In the following, the operational constraints of the ADN and DERs (9) and (10) are defined assuming that:

- dispatchable distributed generators (DDGs) can provide both active/reactive power reserves ($r_{hts}^{\mathrm{DG,P}}$, $r_{hts}^{\mathrm{DG,Q}}$);
- SDGs are sources of active power uncertainties ($\Delta \mathrm{P}_{kts}^{\mathrm{SG}}$) and they can only provide reactive power reserves ($r_{kts}^{\mathrm{SG,Q}}$);
- loads are sources of both active/reactive power uncertainties ($\Delta \mathrm{P}_{its}^{\mathrm{D}}, \Delta \mathrm{Q}_{its}^{\mathrm{D}}$).

1.4.3.2. Modeling the Technical constraints of ADN

The linearized load flow model proposed in [11] is used to derive expressions of:

- the active/reactive power reserve absorbed by ADN from the upper-layer grid, at ADN connection point ($r_{0'ts}^{\mathrm{P}}, r_{0'ts}^{\mathrm{Q}}$),
- voltage magnitudes of all nodes of ADN (V_{jts}),
- current phasor of all branches of ADN (I_{lts}),

as a linear function of the nodal injections $\Delta P_{its}^{\mathrm{Net}}$ and $\Delta Q_{its}^{\mathrm{Net}}$.

The net deviation of the active/reactive power injection at node i from its base case operating point (for the selected time slot t of the next day) during the scenario s can be written as:

$$\Delta P_{its}^{\mathrm{Net}} = -\Delta \mathrm{P}_{its}^{\mathrm{D}} + \sum_{h\in \mathbb{DG}_i} r_{hts}^{\mathrm{DG,P}} + \sum_{k\in \mathbb{SG}_i} \Delta \mathrm{P}_{kts}^{\mathrm{SG}} \qquad \forall i \in \mathbb{B}, \qquad (11)$$

$$\Delta Q_{its}^{\mathrm{Net}} = -\Delta \mathrm{Q}_{its}^{\mathrm{D}} + \sum_{h\in \mathbb{DG}_i} r_{hts}^{\mathrm{DG,Q}} + \sum_{k\in \mathbb{SG}_i} r_{kts}^{\mathrm{SG,Q}} \qquad \forall i \in \mathbb{B}. \qquad (12)$$

The active/reactive power reserves absorbed by the ADN from the upper-layer grid are:

$$r_{0'ts}^{\mathrm{P}} = \mathbf{G}_t^{\mathrm{P0}} + \sum_{i\in \mathbb{B}} \left(\mathbf{G}_{it}^{\mathrm{PP}}\, \Delta P_{its}^{\mathrm{Net}} + \mathbf{G}_{it}^{\mathrm{PQ}}\, \Delta Q_{its}^{\mathrm{Net}}\right) \qquad \forall s \in \mathbb{S}, \qquad (13)$$

$$r_{0'ts}^{\mathrm{Q}} = \mathbf{G}_t^{\mathrm{Q0}} + \sum_{i\in \mathbb{B}} \left(\mathbf{G}_{it}^{\mathrm{QP}}\, \Delta P_{its}^{\mathrm{Net}} + \mathbf{G}_{it}^{\mathrm{QQ}}\, \Delta Q_{its}^{\mathrm{Net}}\right) \qquad \forall s \in \mathbb{S}. \qquad (14)$$

The maximum current flow limit of branch l can be expressed as the following nonlinear constraint:

$$|I_{lts}|^2 = {I_{lts}^{\mathrm{real}}}^2 + {I_{lts}^{\mathrm{imag}}}^2 \leq {\mathrm{I}_l^{\mathrm{Max}}}^2 \qquad \forall l \in \mathbb{L}, \forall s \in \mathbb{S}. \qquad (15)$$

As represented in Fig. 4, the nonlinear constraint (15) is linearized based on a pre-defined number of linear boundaries approximating the real curve:

$$\mathbf{F}_{fl}^{\mathrm{real}} I_{lts}^{\mathrm{real}} + \mathbf{F}_{fl}^{\mathrm{imag}} I_{lts}^{\mathrm{imag}} \leq \mathbf{F}_{fl}^{0} \qquad \forall l \in \mathbb{L}, \forall f \in \mathbb{F}_l, \forall s \in \mathbb{S}, \qquad (16)$$

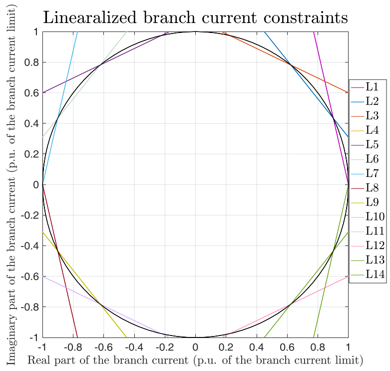

Fig. 4. Linearized branch current constraint.

where the real and imaginary part of the current phasor of branch l[1] are expressed as a linear function of the nodal active/reactive power deviations:

$$I_{lts}^{\mathrm{real}} = \mathbf{H}_{lt}^{0,\mathrm{real}} + \sum_{i\in\mathbb{B}} \left(\mathbf{H}_{lit}^{\mathrm{P,real}}\, \Delta P_{its}^{\mathrm{Net}} + \mathbf{H}_{lit}^{\mathrm{Q,real}}\, \Delta Q_{its}^{\mathrm{Net}}\right) \qquad \forall l \in \mathbb{L}, \forall s \in \mathbb{S}, \qquad (17)$$

$$I_{lts}^{\mathrm{imag}} = \mathbf{H}_{lt}^{0,\mathrm{imag}} + \sum_{i\in\mathbb{B}} \left(\mathbf{H}_{lit}^{\mathrm{P,imag}}\, \Delta P_{its}^{\mathrm{Net}} + \mathbf{H}_{lit}^{\mathrm{Q,imag}}\, \Delta \mathrm{Q}_{its}^{\mathrm{Net}}\right) \qquad \forall l \in \mathbb{L}, \forall s \in \mathbb{S}. \qquad (18)$$

The voltage magnitude of node j can be expressed as a linear function of the nodal active/reactive power deviations. Consequently, the nodal voltage magnitude limits can be linearly modeled as:

$$\mathrm{V}_j^{\mathrm{Min}} \le V_{jts} = \mathbf{E}_{jt}^{0} + \sum_{i\in\mathbb{B}} \left(\mathbf{E}_{jit}^{\mathrm{P}}\, \Delta P_{its}^{\mathrm{Net}} + \mathbf{E}_{jit}^{\mathrm{Q}}\, \Delta Q_{its}^{\mathrm{Net}}\right) \le \mathrm{V}_j^{\mathrm{Max}} \qquad \forall j \in \mathbb{B}, \forall s \in \mathbb{S}. \qquad (19)$$

1.4.3.3. Modeling the capability limits of DERs

The power capability limits of DERs, which are typically nonlinear, are linearized by using a pre-defined number of linear boundaries. For instance, Fig. 5 shows the capability curve of a solar PV plant from [12], and its linearized version. Similarly, Fig. 6 shows the capability curve of a DDG from [13], like a gas turbine.

Based on the linearized models of the capability limits of DDGs and SDGs, the operational constraints of DDG h and SDG k are:

$$\mathbf{K}_{nht}^{0} + \mathbf{K}_{nh}^{\mathrm{P}} r_{hts}^{\mathrm{P}} + \mathbf{K}_{nh}^{\mathrm{Q}} r_{hts}^{\mathrm{Q}} \le 0 \qquad \forall n \in \mathbb{C}_h, \forall h \in \mathbb{DG}, \forall s \in \mathbb{S}, \qquad (20)$$

$$\mathbf{M}_{nkt}^{0} + \mathbf{M}_{nkt}^{\mathrm{P}} \Delta \mathrm{P}_{kts}^{\mathrm{SG}} + \mathbf{M}_{nkt}^{\mathrm{Q}} r_{kts}^{\mathrm{Q}} \le 0 \qquad \forall n \in \mathbb{C}_k, \forall k \in \mathbb{SG}, \forall s \in \mathbb{S}. \qquad (21)$$

1.4.4. On the Convexity of the RPC Area of ADN

Relying on the linearized model of ADN's constraints presented in 1.4.3.2, it is formally proven here that the RPC area is convex. First, the following theorems, proven in appendix, are introduced.

[1] The maximum current flow limit of branch l is modeled for its both sending and receiving ends.

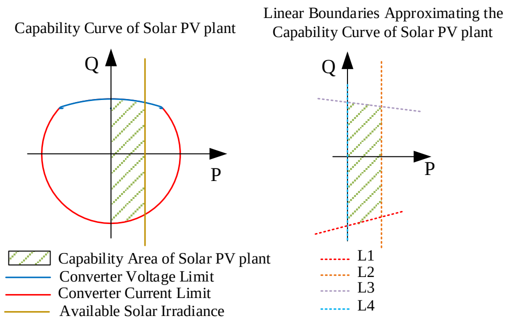

Fig. 5. Capability curve of a solar PV plant.

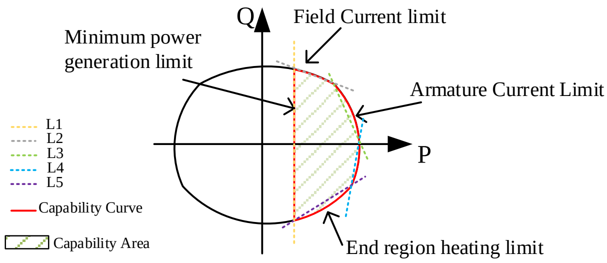

Fig. 6. Capability curve of a DDG.

Theorem 1 Assuming that the capability limits of all DERs [12], [13] of the ADN are convex areas and that the linearized grid model (16)-(19) holds, the RPC area of ADN for a given scenario is a convex area.

Theorem 2 The intersection of convex areas is convex.

Theorem 3 The RPC area of ADN, obtained by considering all scenarios, is convex in the $R^{\mathrm{P}}_{0\prime t} - R^{\mathrm{Q}}_{0^{\prime}t}$ plane.

Based on Theorem 3, the main result of this section is now presented. As, the RPC area is a convex area, it is possible to conclude that linearly interpolating the points as done in Step 3, achieves a conservative feasible approximation of the RPC curve.

2. Achievement of deliverable:

2.1. Date

November 2018

2.2. Demonstration of the deliverable

2.2.1. Case Study

The modified IEEE 33-bus distribution test system [14], shown in Fig. 2, is utilized as the case study to derive the RPC area. The modification refers to the presence of SDGs,

Table I. Characteristics of SDGs.

Solar PV SDGs		Wind SDGs	
Connected to node	Nominal power (kVA)	Connected to node	Nominal power (kVA)
5, 22	300	11	300
14, 20	350	16, 26	450

Table II. Characteristics of DDGs.

Connected to node	Nominal power (kVA)	Minimum active power generation limit (kW)
3, 9	500	10
17, 31	700	20

composed by solar PV and wind generators, and DDGs. The characteristics of SDGs and DDGs are given in Table I and Table II, respectively. The solar PV and load profiles, for 24 hours of study, are real measurements from a monitored primary high-to-medium voltage substation in the south of Switzerland. The wind profiles are from [15]. The loads are assumed voltage-independent and with power factor equal to 0.95. Injections of both SDGs and DDGs are also assumed voltage-independent. Statutory minimum/maximum voltage limits are chosen as 0.95 pu and 1.05 pu.

It is assumed that the day-ahead forecast errors of the nodal active power consumption/generation are independent and identically distributed. The active power forecast error of each load is sampled from a normal distribution with 0 mean and such that the standard deviation of the total load forecast error is 3% of the total load of the ADN, as in [16]. The deviation of active power generation of each SDG from its forecasted value is sampled from a normal distribution with 0 mean and such that the standard deviation of the whole system stochastic generation forecast error is 7% of the total system stochastic generation forecast, as in [17]. This approach is used to model the uncertainties by generating 2500 scenarios.

The problem is modelled by using YALMIP-MATLAB [18] and solved with GUROBI [19] on a Windows based system with a 2.8 GHz Xeon CPU and 32 GB of RAM.

2.2.2. Impact of the granularity on the estimated RPC Area

The impact of the granularity on the precision of the estimated RPC area and on the computation time is investigated by choosing several values of granularity. Fig. 7 shows the surface the RPC area and computation time for the first time slot of the day as a function of the granularity. It shows that, by increasing the granularity, the precision of the estimated RPC area improves at the cost of a higher computation time. However, when above 400 kVA, the precision of the estimated RPC does not change considerably, while the

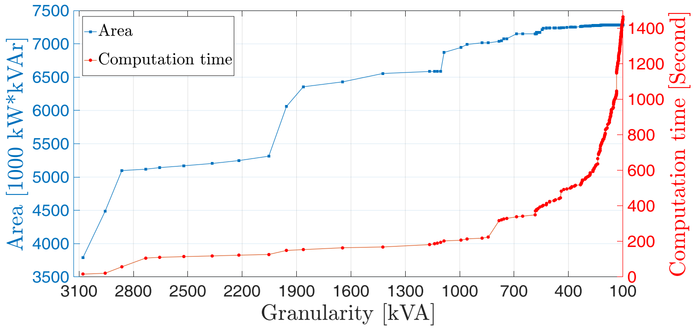

Fig. 7. Impact of the defined granularity on the precision of estimated RPC and its computation time.

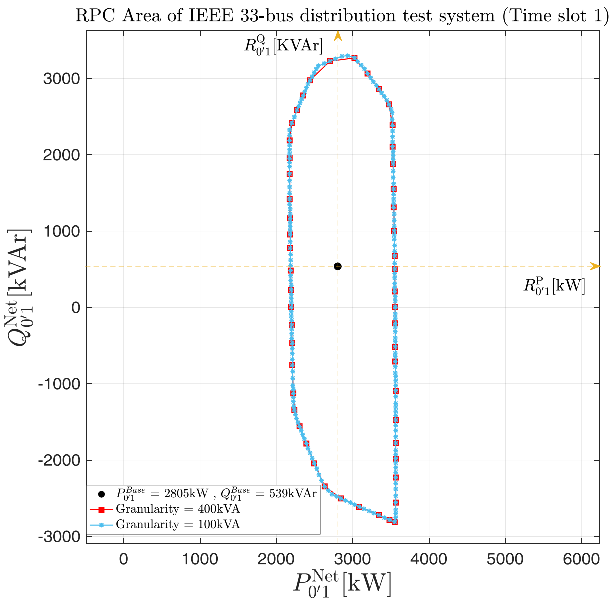

Fig. 8. Estimated RPC area for the maximum granularity equal to 100 kVA and 400 kVA.

computation drastically increases. Therefore, in the following analysis, 400 kVA is retained as the value of granularity as it achieves a trade-off between degree of approximation and computational time. The estimated RPC areas for granularity values of 400 kVA and 100 kVA are shown in Fig. 8. As it can be seen, the two RPC areas are similar, thus denoting that, in this case, the lower granularity achieves a good degree of approximation.

2.2.3. Evolution over time of the estimated RPC Areas

The RPC areas of the ADN are estimated for all 24 time slots of study and are shown in **Error! Reference source not found.**. In this figure, the RPC areas are represented in $R^{\mathrm{P}}_{0't} - R^{\mathrm{Q}}_{0't}$ plane instead of $P^{\mathrm{Net}}_{0't} - Q^{\mathrm{Net}}_{0't}$ to better highlight the evolution of the RPC areas over the period of study. As it can be seen, the RPC areas of all time intervals have different shapes, denoting that integrating forecasting scenarios is critical to achieve an accurate representation of the dynamic capacity of ADNs for reserve provision. As expected, the RPC areas shown in Fig. 9 are convex, therefore they can be embedded efficiently in existing convex optimization tools [20] used by operators for optimal allocation of power reserves without impacting on

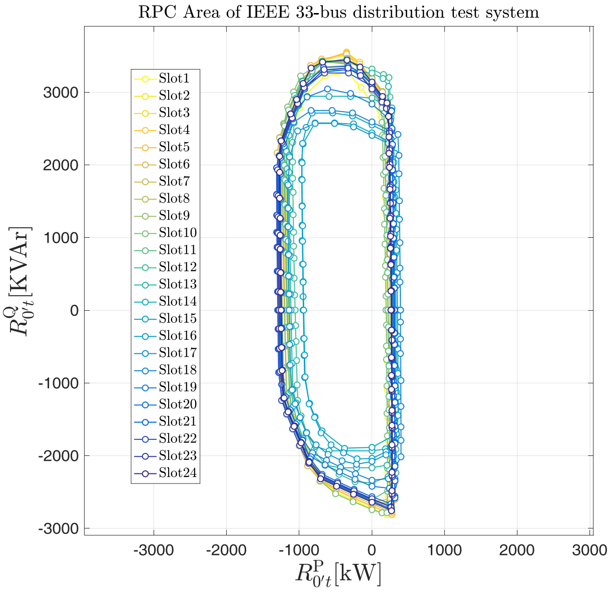

Fig. 9. The superimposed RPC area of all 24 time slots of study.

their tractability. The RPC area of each time slot is estimated in less than 500 seconds. For each estimated point of the RPC curve and for each time interval, the feasibility of the problem was verified with a conventional nonlinear load flow, revealing that grid constraints were violated in less than 0.001% of the cases.

3. Impact

This deliverable introduced a method to estimate the RPC area of ADNs for a desired time horizon while considering forecast errors, and operational constraints of the grid (i.e., nodal voltages and line currents) and DERs. Based on the method introduced in this deliverable, we will develop:

1- a method for re-dispatching (in real-time operation) the DERs of ADN in such a way that the requested ancillary services by the upper-layer grid operator is provided at the ADN connection point.

2- A method for characterizing the RPC area of regional energy networks at the TSO-DSO connection point by aggregating the RPC areas of ADNs at the sub-transmission level.

Appendix

Proof of Theorem 1: Let $\boldsymbol{X}_{ts} = [\Delta P_{1ts}^{\mathrm{Net}}, \dots, \Delta P_{\mathrm{N}_{\mathbb{B}}ts}^{\mathrm{Net}}, \Delta Q_{1ts}^{\mathrm{Net}}, \dots, \Delta Q_{\mathrm{N}_{\mathbb{B}}ts}^{\mathrm{Net}}]^{\mathrm{T}}$ denote the vector of the operating point of the ADN collecting the deviations of the nodal active/reactive power injections. For the given operating point $\boldsymbol{X}_{ts}$, the corresponding point $[r_{0'ts}^{\mathrm{P}}, r_{0'ts}^{\mathrm{Q}}]^{\mathrm{T}}$ in the $R_{0't}^{\mathrm{P}} - R_{0't}^{\mathrm{Q}}$ plane can be calculated using (13) and (14). Contrariwise, for the given point $[r_{0'ts}^{\mathrm{P}}, r_{0'ts}^{\mathrm{Q}}]^{\mathrm{T}}$, the corresponding operating point $\boldsymbol{X}_{ts}$ can be calculated as:

$$\Delta P_{its}^{\mathrm{Net}} = \mathbf{G}'^{\mathrm{P0}}_{t} + \sum_{i\in\mathbb{B}} \left(\mathbf{G}'^{\mathrm{PP}}_{it}\, r_{0'ts}^{\mathrm{P}} + \mathbf{G}'^{\mathrm{PQ}}_{it}\, r_{0'ts}^{\mathrm{Q}}\right) \qquad \forall i \in \mathbb{B} \tag{A.1}$$

$$\Delta Q_{its}^{\mathrm{Net}} = \mathbf{G}'^{\mathrm{Q0}}_{t} + \sum_{i\in\mathbb{B}} \left(\mathbf{G}'^{\mathrm{QP}}_{it}\, r_{0'ts}^{\mathrm{P}} + \mathbf{G}'^{\mathrm{QQ}}_{it} r_{0'ts}^{\mathrm{Q}}\right) \qquad \forall i \in \mathbb{B}. \tag{A.2}$$

Operating point $\boldsymbol{X}_{ts}$ is said *feasible* if it satisfies the capability limits of all DERs and the operational constraints of the ADN in (16) and (19).

Based on the above-mentioned notations and definitions along with the assumptions of theorem, the goal here is to show that for each two given points 1 and 2 belonging to the RPC area of scenario *s*, all points located on the line connecting them to each other also belong to that RPC area. Each point located on this line like point 3 can be mathematically represented as (hereafter superscripts 1,2 and 3 denote the index of points):

$$\begin{bmatrix} {r_{0'ts}^{\mathrm{P}}}^{3} \\ {r_{0'ts}^{\mathrm{Q}}}^{3} \end{bmatrix} = (1-\alpha)\begin{bmatrix} {r_{0'ts}^{\mathrm{P}}}^{1} \\ {r_{0'ts}^{\mathrm{Q}}}^{1} \end{bmatrix} + \alpha \begin{bmatrix} {r_{0'ts}^{\mathrm{P}}}^{2} \\ {r_{0'ts}^{\mathrm{Q}}}^{2} \end{bmatrix}. \tag{A.3}$$

where α is a constant between 0 and 1.

Combination of (A.1)-(A.3) yields:

$${\boldsymbol{X}_{ts}}^{3} = (1-\alpha){\boldsymbol{X}_{ts}}^{1} + \alpha{\boldsymbol{X}_{ts}}^{2}. \tag{A.4}$$

Note that points 1 and 2 belong to the RPC area and they are feasible, thus, it can be inferred that:

1- Points ${\boldsymbol{X}_{ts}}^{1}$ and ${\boldsymbol{X}_{ts}}^{2}$ satisfy the capability limits of all DERs limits.

2- Points ${\boldsymbol{X}_{ts}}^{1}$ and ${\boldsymbol{X}_{ts}}^{2}$ satisfy the nodal voltage constraint of ADN. Based on (19), it can be mathematically expressed for each node like *j* as:

$$\mathrm{V}_{j}^{\mathrm{Min}} \le \mathbf{E}_{jt}^{0} + \sum_{i\in\mathbb{B}} \left(\mathbf{E}_{jit}^{\mathrm{P}}\, \Delta P_{its}^{\mathrm{Net}^{1}} + \mathbf{E}_{jit}^{\mathrm{Q}}\, \Delta Q_{its}^{\mathrm{Net}^{1}}\right) \le \mathrm{V}_{j}^{\mathrm{Max}} \tag{A.5}$$

$$\mathrm{V}_j^{\mathrm{Min}} \leq \mathbf{E}_{jt}^{0} + \sum_{i \in \mathbb{B}} \left(\mathbf{E}_{jit}^{\mathrm{P}} \, \Delta P_{its}^{\mathrm{Net}^2} + \mathbf{E}_{jit}^{\mathrm{Q}} \, \Delta Q_{its}^{\mathrm{Net}^2} \right) \leq \mathrm{V}_j^{\mathrm{Max}}. \qquad (\mathrm{A.6})$$

3- Points ${\boldsymbol{X}_{ts}}^1$ and ${\boldsymbol{X}_{ts}}^2$ satisfy the maximum current flow limits of all branches. Based on (16), it can be mathematically expressed for each branch like *l* as:

$$\mathbf{F}_{fl}^{\mathrm{real}} {I_{lts}^{\mathrm{real}}}^1 + \mathbf{F}_{fl}^{\mathrm{imag}} {I_{lts}^{\mathrm{imag}}}^1 \leq \mathbf{F}_{fl}^{0} \qquad \forall f \in \mathbb{F}_l \qquad (\mathrm{A.7})$$

$$\mathbf{F}_{fl}^{\mathrm{real}} {I_{lts}^{\mathrm{real}}}^2 + \mathbf{F}_{fl}^{\mathrm{imag}} {I_{lts}^{\mathrm{imag}}}^2 \leq \mathbf{F}_{fl}^{0} \qquad \forall f \in \mathbb{F}_l. \qquad (\mathrm{A.8})$$

1) Proof of ${\boldsymbol{X}_{ts}}^3$ satisfies the capability limits of DERs:

Both ${\boldsymbol{X}_{ts}}^1$ and ${\boldsymbol{X}_{ts}}^2$ satisfy the capability limits of all DERs. Since capability limits of DERs are assumed to be convex areas, thus any point like ${\boldsymbol{X}_{ts}}^3$ defined based on (A.4) satisfies these capability limits.

2) Proof of ${\boldsymbol{X}_{ts}}^3$ satisfies the nodal voltage constraint of ADN:

It is shown that for the given points ${\boldsymbol{X}_{ts}}^1$ and ${\boldsymbol{X}_{ts}}^2$ respectively satisfying (A.5) and (A.6), any point like ${\boldsymbol{X}_{ts}}^3$ defined based on (A.4) satisfies (19). To this end, first (A.5) and (A.6) are respectively multiplied by $(1-\alpha)$ and α, then they are added to each other and composed with (A.4) yielding:

$$\mathrm{V}_j^{\mathrm{Min}} \leq \mathbf{E}_{jt}^{0} + \sum_{i \in \mathbb{B}} \left(\mathbf{E}_{jit}^{\mathrm{P}} \, \Delta P_{its}^{\mathrm{Net}^3} + \mathbf{E}_{jit}^{\mathrm{Q}} \, \Delta Q_{its}^{\mathrm{Net}^3} \right) \leq \mathrm{V}_j^{\mathrm{Max}} \qquad (\mathrm{A.9})$$

Expression (A.9) demonstrates that ${\boldsymbol{X}_{ts}}^3$ satisfies the nodal voltage constraint of ADN.

3) Proof of ${\boldsymbol{X}_{ts}}^3$ satisfies the maximum current flow limits of all branches:

Considering the given points ${\boldsymbol{X}_{ts}}^1$ and ${\boldsymbol{X}_{ts}}^2$ respectively satisfying (A.7) and (A.8), it is shown that any point like ${\boldsymbol{X}_{ts}}^3$ defined based on (A.4) satisfies (16). To this end, first (A.7) and (A.8) are respectively multiplied by $(1-\alpha)$ and α, then they are added to each and composed with (17), (18) and (A.4) yielding:

$$\mathbf{F}_{fl}^{\mathrm{real}} {I_{lts}^{\mathrm{real}}}^3 + \mathbf{F}_{fl}^{\mathrm{imag}} {I_{lts}^{\mathrm{imag}}}^3 \leq \mathbf{F}_{fl}^{0} \qquad \forall f \in \mathbb{F}_l. \qquad (\mathrm{A.10})$$

Expression (A.10) demonstrates that ${\boldsymbol{X}_{ts}}^3$ satisfies the maximum current flow limits of all branches.

Based on the above-mentioned proofs, it is trivial that ${\boldsymbol{X}_{ts}}^3$ is a feasible points and consequently $\left[{r_{0'ts}^{\mathrm{P}}}^3, {r_{0'ts}^{\mathrm{Q}}}^3\right]^{\mathrm{T}}$ belongs to the RPC area of ADN. ■

Proof of Theorem 2: If the intersection is empty, or consists of a single point, the theorem is true. Otherwise, select any two points 1 and 2 in the intersection. The line connecting these points must also lie in all areas, thus must lie within their intersection. ■

Proof of Theorem 3: The method introduced in **Error! Reference source not found.** defines the boundary of the RPC area, in each direction θ (as shown in **Error! Reference source not found.**), as the minimum amount of reserve that ADN can provide over all scenarios. It can be mathematically expressed as:

$$A_{\mathbb{S}}^{\mathrm{RPC}} = \bigcap_{s \in \mathbb{S}} A_s^{\mathrm{RPC}}, \tag{A.11}$$

where $A_{\mathbb{S}}^{\mathrm{RPC}}$ indicate the RPC area obtained by considering all scenarios belong to $\mathbb{S}$, A_s^{RPC} indicate the RPC area obtained by considering single scenario s and Operator ∩ calculates the intersection of all areas.

On the one hand, Theorem 1 proved that A_s^{RPC} is convex for each scenario s. On the other hand, theorem 2 proved that the intersection of a number of convex areas returns a convex area. Thus, it is trivial that $A_{\mathbb{S}}^{\mathrm{RPC}}$ is convex. ■

References

[1] E. Scolari, F. Sossan, M. Paolone, "Irradiance prediction intervals for PV stochastic generation in microgrid applications," *Solar Energy,* 139, pp.116-129, Oct. 2016.

[2] Y. G. Rebours, D. S. Kirschen, M. Trotignon, and S. Rossignol, "A survey of frequency and voltage control ancillary services—part I: Technical features," *IEEE Trans. Power Syst.*, vol. 22, no. 1, pp. 350–357, Feb. 2007.

[3] "Grid integration of large capacity renewable energy sources and use of large-capacity electrical energy storage." *IEC White Paper, Geneva, Switzerland* 2012, [Online]. Available: http://www.iec.ch/whitepaper/pdf/ iecWP-gridintegrationlargecapacity-LR-en.pdf

[4] M. CAILLIAU and J. A. OGANDO, "Integrating Intermittent Renewable Sources in the EU Electricity System by 2020: Challenges and Solutions, *Eurelectric. Brussels, Belgium* 2010.

[5] M. Heleno, R. Soares, J. Sumaili, R.J. Bessa, L. Seca, and M. A. Matos, "Estimation of the flexibility range in the transmission-distribution boundary," in Proc. IEEE Eindhoven Power Tech, Jun. 2015, pp. 1-6.

[6] F. Capitanescu, "TSO–DSO interaction: Active distribution network power chart for TSO ancillary services provision," *Elect. Power Syst. Res.*, Vol. 163, Part A, pp. 226-230, Oct. 2018.

[7] J. P. Silva, J. Sumaili, R.J. Bessa, L. Seca, M. A. Matos, V. Miranda, M. Caujolle, B. Goncer-Maraver and M. Sebastian-Viana, "Estimating the active and reactive power flexibility area at the TSO-DSO interface,", *IEEE Trans. Power Syst.*, Feb. 2018.

[8] J. Silva, J. Sumaili, R. J. Bessa, L. Seca, M. Matos and V. Miranda, "The challenges of estimating the impact of distributed energy resources flexibility on the TSO/DSO boundary node operating points". Computers & Operations Research, Vol 96, pp. 294-304, August 2018.

[9] H .Gerard, E. Rivero and D. Six, "Basic schemes for TSO-DSO coordination and ancillary services provision," Smartnet, 2016, [Online]. Available: http://smartnet-project.eu/wp-content/uploads/2016/12/D1.3_20161202_V1.0.pdf.

[10] P. Mandatova, O. Mikhailova, "Flexibility and Aggregation Requirements for their

interaction in the market," Eurelectric. Brussels, Belgium 2014, [Online]. Available: https://www.usef.energy/app/uploads/2016/12/EURELECTRIC-Flexibility-and-Aggregation-jan-2014.pdf

[11] A. Bernstein, and E. Dall'Anese. "Linear power-flow models in multiphase distribution networks." *IEEE PES Innovative Smart Grid Technologies Conference Europe*, Jan. 2017.

[12] A. Cabrera-Tobar, E. Bullich-Massagué, M. Aragüés-Peñalba, O. Gomis-Bellmunt, "Capability curve analysis of photovoltaic generation systems" *Solar Energy,* 140, pp.255-264, Nov. 2016.

[13] P. Kundur, J. B. Neal, and G. L. Mark. "*Power system stability and control*," McGraw-hill, New York, 1994.

[14] M. E. Baran and F. Wu. "Network reconfiguration in distribution systems for loss reduction and load balancing." *IEEE Trans. on Power delivery,* Vol. 4, No..2, pp. 1401-1407, April 1989.

[15] "Homer Energy." [Online]. Available: http://homerenergy.com/

[16] M. Bozorg, F. Sossan, J. Y. Le Boudec, and M. Paolone, "Influencing the bulk power system reserve by dispatching power distribution networks using local energy storage". *Elect. Power Syst. Res.*, 163, pp.270-279, June 2018.

[17] M. Kalantar, M. Bozorg, F. Sossan, R. Cherkaoui, "Allocation of Frequency Control Reserve from Aggregated Resources of Active Distribution Systems". *In Power Syst. Computation Conf.*, Dublin, Ireland, Jun., 2018.

[18] J. Löfberg, "YALMIP: A toolbox for modeling and optimization in MATLAB," *in Proc. CACSD Conf.*, Taipei, Taiwan, pp. 284–289, 2004.

[19] "*Gurobi Optimizer Reference Manual*," Gurobi Optimization, Inc. [Online]. Available: http://www.gurobi.com.

[20] L. Bam, and W. Jewell. "Power system analysis software tools." *IEEE Power Engineering Society General Meeting,* San Francisco, USA, 2005.